



Mechanical behavior analyses of 4D printed metamaterials structures with excellent energy absorption ability

Wei Zhao^a, Chengbin Yue^a, Liwu Liu^a, Jinsong Leng^b, Yanju Liu^{a,*}

^a Department of Astronautical Science and Mechanics, Harbin Institute of Technology (HIT), P.O. Box 301, No. 92 West Dazhi Street, Harbin 150001, People's Republic of China

^b Center for Composite Materials and Structures, Harbin Institute of Technology (HIT), P.O. Box 3011, No. 2 YiKuang Street, Harbin 150080, People's Republic of China

ARTICLE INFO

Keywords:

Shape memory
4D printing
Shape-transformation
Metamaterials
Energy absorption

ABSTRACT

Mechanical metamaterials with immense specific energy absorption and high specific strength are extensively being applied in engineering fields, including bone tissue scaffolds, aerospace and automotive engineering. Many structural design strategies have been developed to improve their mechanical properties. The lattice metamaterials with a tremendous specific energy absorption capacity exhibit continual platform stress after initial yield and before densification. Here, combined with bionic design, we designed and fabricated a series of mechanical metamaterial with tension-dominated mechanical behavior which can assimilate enormous amounts of energy while maintaining a low density. The design strategy relied on the network construction in the periodic grid topology, which took the microstructure with several beams as the building block connecting the grid nodes. The mechanical properties can be adjusted by changing topology parameters. Additionally, the metamaterials fabricated by 4D printing technology show intelligent properties, which can jump from one mode to another under external stimulation. It was worth mentioning that the shape memory effect (SME) also endowed the material with certain self-healing properties. Excellent compressive resistance, energy absorption, shock absorption and shape memory effect suggest the application prospect in engineering fields.

1. Introduction

Absorbing mechanical shock and the vibration energy is a necessary factor that needs to be considered in industrial design. Mechanical metamaterials, owing to their light weight, high energy absorption capacity and excellent crashworthiness, have gained broad applications in various fields. Mechanical metamaterials aim to achieve fantastic mechanical properties by optimizing the design of the structure [1,2]. The unique properties, including negative Poisson's ratio [3], bistable state [4], deformable [5], negative compression coefficient [1], negative stiffness [6], crumpling-based soft metamaterials [7] and tunable negative thermal expansion, stem from the rational design at the microscopic scale.

For most of the structures, the mechanical properties including the impact resistance will weaken with the decrease of the relative density [8]. However, the mechanical target of light weight and high strength, and high energy absorption efficiency can be realized by efficient structure design and parameter adjustment [9]. For example, Jang et al. [10] developed a kind of mechanical metamaterial composed of the

tetrahedral structural unit based on kelvin foam and achieved extraordinary compressive strength. By investigating the mechanical property of Miura-origami, Wei et al. [11] developed a structure that had a negative Poisson ratio and excellent deformation performance. Using liquid crystal elastomer (LCE) and periodic single cell structure design, Yu et al. fabricated a series of LCE-based lattice structures with dramatically enhanced energy dissipation [12–14].

As a kind of typical mechanical metamaterial, the micro-truss lattice is a periodic structure composed of nodes and truss elements, which has obtained huge attention in the territory of shock absorption and energy absorption [15]. The mechanical properties are determined by the number and configuration of truss elements [16]. According to topological criteria, they can be segmented into bending-dominated or tension-dominated structures [17]. With the development of micro-fabrication and nano-manufacturing technology, the lattice structure is able to be fabricated by the trusses with a diameter ranging from submicron to millimeters [18].

Up to now, for energy-absorbing metamaterials, most of the high energy absorption capacity is realized through different geometric

* Corresponding author.

E-mail address: yj_liu@hit.edu.cn (Y. Liu).

designs [19]. However, the rational designs are not limited to the geometry scale, but also include geometric configuration and material selection. For example, by introducing bionic concepts into the design, the structures will have a better ability to adapt to the environment [20]. Additionally, if the metamaterials are fabricated by intelligent materials, such as shape memory polymer (SMP) [21–27], they will be equipped with excellent environmental adaptability and a large deformation capacity.

Generally, once the critical buckling load is reached, the structure will be damaged and affect the function of energy absorption and shock absorption. This kind of structure only exhibits high strength and energy absorption efficiency under low density, but there is no special function attached to it. If mechanical compression [28,29], expansion [30], and magnetic [31] are used to trigger the pattern switching, reversible and repeatable shape transformation can be realized by restructuring the topological units. It is interesting to imagine that if pattern switching [32] can be triggered, the structure could be designed to respond to different environmental changes, even exhibiting some self-repairing function [33].

Here, we designed a series of lattice metamaterials with excellent energy absorbing capacity. The mechanical properties can be adjusted by varying the topological parameters including the diameters of the truss, and the ratio of length to height. It was worth noting that the design of the gradient structure was presented by combining the unit-cell with different mechanical properties. Utilizing SMP as the feed material, the lattice metamaterials were fabricated using 4D printing [34–37]. Subsequently, the crushing performance was evaluated and analyzed by compressive tests. Based on the SME of SMP, the shape transformation experiments were conducted and compared with simulation results.

2. Materials and methods

2.1. Bionics design of truss

Bamboo is a typical organism existing in nature with good mechanical properties. It has a series of advantages including high strength, good elasticity, stable performance and low density. The unique structure of the culm wall is the material basis of the excellent mechanical properties of bamboo. A variety of cells with different morphological structures can be distinguished from the culm wall. However, from the mechanical point, these cells can be divided into two categories: The first type is the basic tissue cells, which are round thin-walled structures under the microscope and play the role of load transmission; The second type is sclerotic cells with vascular bundles as the main body, which are surrounded by basic tissue cells and responsible for load bearing as shown in Fig. 1(a). For the structural form of bamboo, the bionic design of cylindrical components is intuitive. Fig. 1(b) reveals the evolution of the bamboo cross-section structure. Fig. 1(c) displays the simplified microstructure of the bamboo cross-section. Combined with the bionic design, the bamboo cross-section can be simplified into the form of a hollow truss.

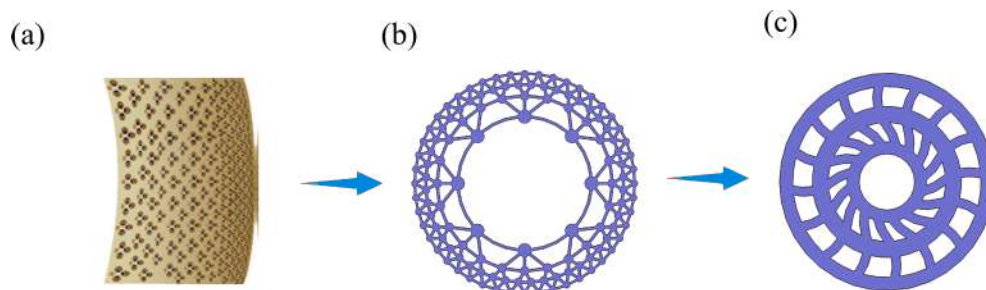


Fig. 1. (a) The microstructure of bamboo cross-section (b) Bionic structure of the cross-section of bamboo (c) Simplified cross-section of bamboo structure.

2.2. Design of the lattice meta-materials structures

For large bone defects and the bone defect site with large bearing capacity, such as the skull, the energy absorption performance is one of the mechanical properties of bone tissue scaffolds to be considered. One of the key parameters is the ratio of the actual volume of material to the entire volume of the structure for energy-absorbing metamaterials. The rational distribution of the materials can make the structure deform uniformly. The simplest choice is the isotropic solid material. However, to make the material get higher utilization efficiency, it is necessary to reduce the actual proportion of the material to introduce some light-weight design.

In this work, three different unit-cell structures were designed. The diagrammatic drawing of the unit cell and the $3 \times 3 \times 3$ representative structures obtained by the topology design were demonstrated in Fig. 2. The length, width, and height were defined as a , a and b for a unit cell, and the truss element in the unit cell had a uniform diameter d . There were 20, 32, and 24 trusses in the unit cells I, II and III, respectively. Unit cells I and II comprised four types of trusses and were defined as 1, 2, 3 and 4 respectively. There were three types of trusses in unit-cell III and defined as 1, 2, and 3, respectively. Arraying them along the x , y , and z directions can produce a lattice structure.

By changing the topological parameters of the trusses, the configuration and the mechanical properties of the structure will be changed and affected. In this work, several different structures were designed by changing the diameter of the trusses to explore the relationship between topological parameters and mechanical properties.

(1) The dimension of the unit-cell was $a = b = 5$ mm. By changing the diameter of the truss, three types with $d = 0.5$, $d = 0.75$ and $d = 1$ were designed. The structures with $9 \times 9 \times 9$ unit cells were obtained by arraying along the x , y and z directions, as shown in Fig. 3(a).

(2) Set $\alpha = b/a$, by changing the parameter α , we have designed two types of unit-cell with $\alpha = 1.5$ and $\alpha = 2$, and the diameter of the truss was $d = 0.5$. Arraying along with x , y and z directions, the obtained structures were shown in Fig. 3(b).

(3) Plants, animals, and other organisms in nature have gradually evolved gradient organizations to adapt to the living environment, which is a highly evolved form. The human bone, for example, is a typical gradient structure, which is divided into the cortical bone and cancellous bone [38]. From the inside to the surface, the human bone changes from cancellous bone to cortical bone, which enables the surface hard and the inner skeleton to be more flexible. By changing the topological parameters, the mechanical properties can be locally controlled to meet different requirements. The functionally graded structures can be accurately fabricated based on the 4D printing technology, which can achieve gradient mechanical properties according to the mapping relationship. The different unit-cell endows the structure with disparate mechanical properties. By varying the type of the unit cell, the functionally graded lattice was constructed (Fig. 3(c)).

In this work, by changing the parameters d , α and unit-cell type, we designed three kinds of gradient structures. For the first type of structure, the upper three layers were comprised of the unit-cell with $a = b =$

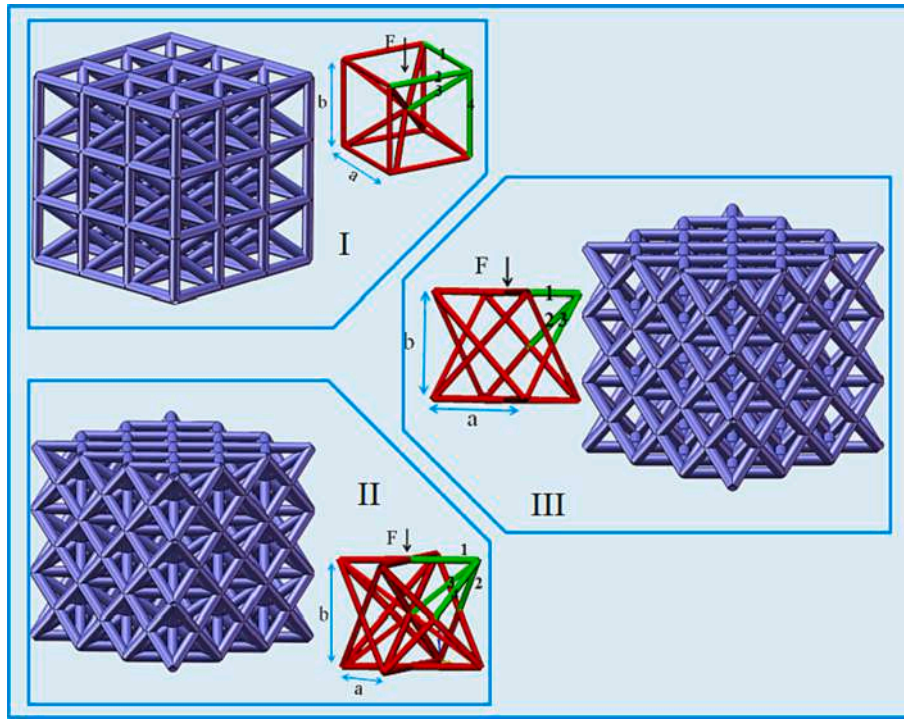


Fig. 2. Schematic of the lattice *meta*-materials structures and representative topological unit-cell.

0.5 mm and $d = 0.5$; The middle three layers were comprised of the unit-cell with $a = b = 0.5$ mm and $d = 0.75$; and the bottom three layers were composed of the unit-cell with $a = b = 0.5$ mm and $d = 1$. For the second type of structure, the upper three layers, the middle three layers and the bottom three layers were comprised of the unit-cell with $x = 1$, $x = 1.5$ and $x = 2$, respectively. For the third type of structure, the upper three layers, the middle three layers and the bottom three layers were comprised of the unit-cell S-I-1–0.5, S-II-1–0.5 and S-III-1–0.5, respectively.

2.3. Fabrication process

A photocuring 3D printer (Anycubic Photon) and a fused deposition modeling 3D printer (Anycubic) were employed to fabricate the shape-transformation *meta*-materials structures. The photosensitive resin and the shape memory printing filament were provided by the Center for Composite Materials and Structures, Harbin Institute of Technology (HIT). The testing of the mechanical properties can be seen in [Supporting Information](#). The exposure time at the bottom of the structure was set as 80 s, the normal exposure time was 23 s, and the spatial resolution was 0.1 mm (detailed processing parameters can be found in [Table S1](#)). The fabricated structures are shown in [Fig. 4](#), which corresponds to (a), (b) and (c) in [Fig. 3](#), respectively.

2.4. Measurement of the Poisson's ratio

The Poisson's ratio was measured by the digital speckle correlation measurement system. The acquisition of real-time image acquisition was finished by the CCD digital camera. Each image was discretized into a gray matrix of 1280×1024 (pixels) and calculated by corresponding software. Furthermore, the measured structure was sprayed with black and white paint as speckles to provide grayscale matching characteristics.

2.5. Energy absorption test

One of the potential applications of this structure is energy

absorption structure and systems [39–41]. If the structure has a high density, the target strength may be achieved. However, its weight efficiency will inevitably be lost. Therefore, suitable parameters are important to achieve higher energy absorption, and the key is the design of a lightweight structure with efficient and practical application value.

The quasi-static compression tests were conducted to evaluate the lattice structure's compressive performance including deformation mode and related crushing performance parameters. The Zwick-010 universal testing machine was employed to conduct quasi-static compressive tests. To ensure the compressive process was quasi-static, the preloading loading speed of 0.5 mm/min was first applied, then the normal loading speed of 5 mm/min was leveraged as a constant. Subsequently, the energy absorption efficiency was evaluated, and the crush performance parameters were calculated.

For lattice metamaterial, the analytical expression of its relative density can be expressed as:

$$\bar{\rho} = \frac{V_m}{V_s} \quad (1)$$

where V_m is the volume occupied by the material entity, and V_s is the overall volume of the metamaterials. The normalized expression of the elastic modulus is adopted to compare the mechanical performances of different structures. The elastic modulus can be expressed as:

$$E = E_s / E_m \quad (2)$$

where E_s is the elastic modulus of the structure, and E_m is the elastic modulus of the material. Normalized compressive stress can be expressed as:

$$\sigma = \sigma_s / \sigma_{mY} \quad (3)$$

where σ_s is the yield strength of the structure, and σ_{mY} is the yield strength of the material. According to the elastoplastic analysis, the first peak value of the stress–strain curve is defined as the yield strength.

The crushing performance parameters are derived from the engineer strain-engineering stress curve. Nominal compressive strain and stress are expressed as $\varepsilon = \delta/H$ and $\sigma = F/A$. δ is the displacement of compression, F is the crushing load, H is the height of the structure, and

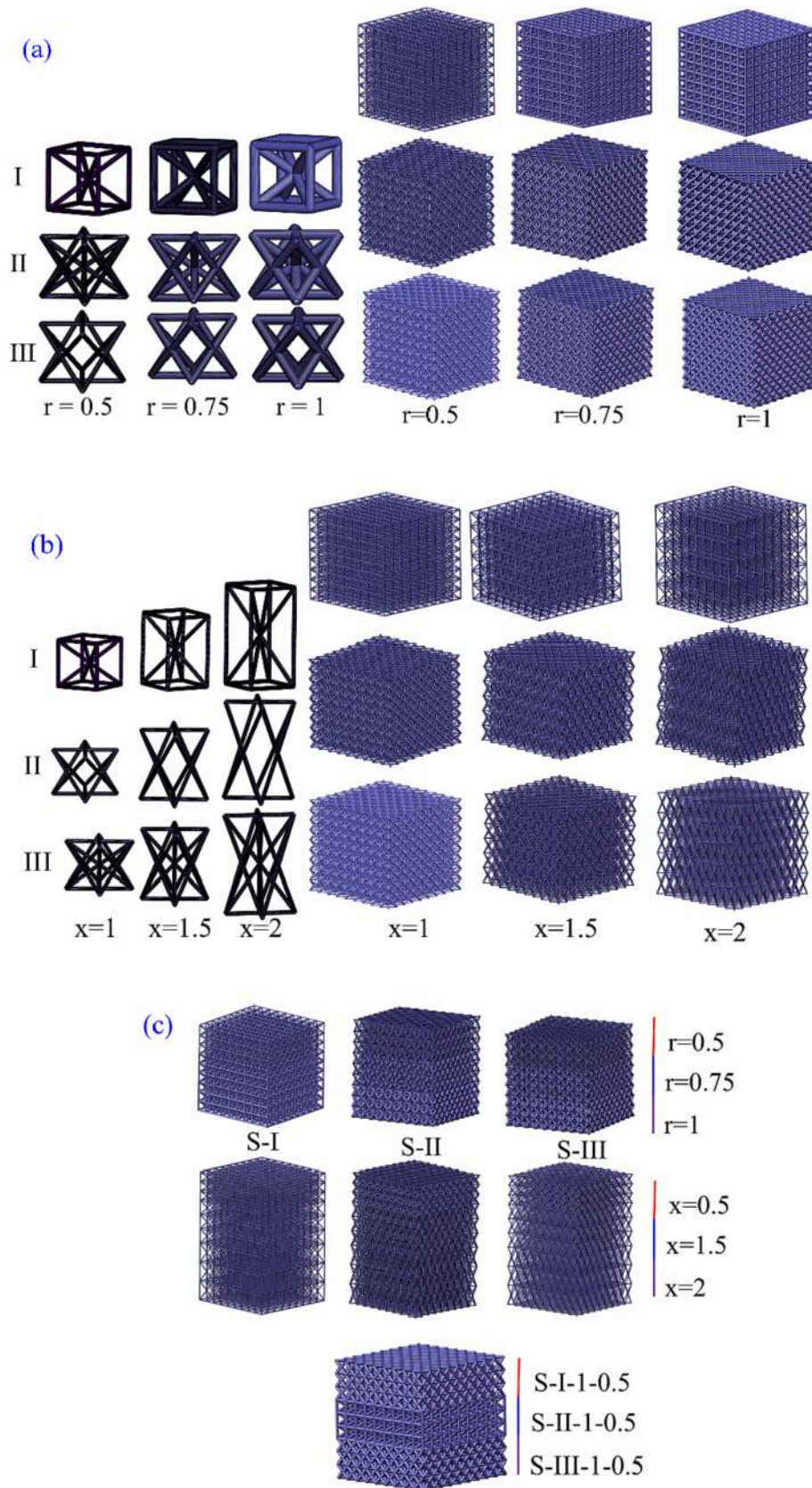


Fig. 3. Schematics of the representative unit cell and the *meta-materials* structures with $9 \times 9 \times 9$ unit cells: *meta-materials* with (a) Different diameters of the beam (b) different ratios of length and height (c) Gradient structure.

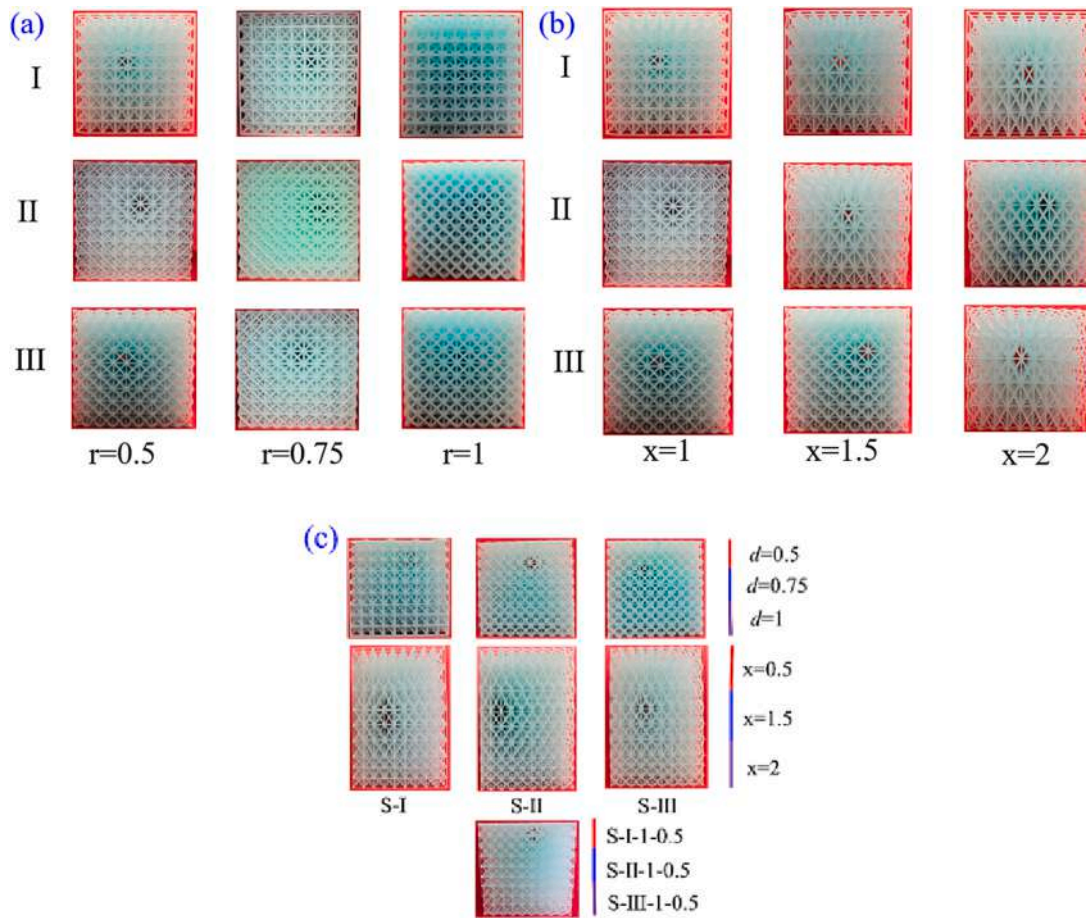


Fig. 4. Shape-transformation *meta*-materials structures fabricated by 4D printing (a) Structures with different diameters of the truss (b) Structures with different ratios of length and height (c) Gradient structure.

A is the crossing section area of the structure. The total energy absorption (EA) is calculated according to the area of the stress–strain curve, and can be expressed as:

$$EA = V \int_0^b \sigma d\varepsilon \quad (4)$$

where b is the displacement of the sample. Specific energy absorption (SEA) is the rate of EA to sample weight (m).

$$SEA = \frac{V \int_0^b \sigma d\varepsilon}{m} \quad (5)$$

Crushing efficiency (CFE) refers to the ratio of average crushing force (MCF) to peak crushing force (PCF), which can be computed as follows:

$$MCF = \frac{1}{b} \int_0^b F \cdot d\delta \quad (6)$$

$$CFE = \frac{MCF}{PCF} \quad (7)$$

2.6. Finite element analysis

A series of *meta*-material models were established by the commercial finite element software ABAQUS. The first-order solid elements C3D8R were adopted to mesh the model. The material properties were assumed to be isotropic and viscoelastic. The generalized Maxwell model was utilized to depict the shape memory behavior. The related parameter was obtained by uniaxial tensile experiments (Supporting Information). The Poisson’s ratio of the material was set as 0.38.

3. Results and discussion

3.1. Meso- and microstructural analysis

The microscopic images of the sample were monitored by scanning electron microscope (SEM, ZIESS Ultra-55). As shown in Fig. 5, the surface of the sample was smooth, the diameter of the beam was a uniform size, and there was no obvious defect. The related physical parameters for *meta*-materials structures were summarized in Table 1, the maximum relative density was 27.74 % of S-II-1–1, and other structures were less than 20 %, which meant that the porosity of the structures was above 80 % except for structure S-II-1–1. The remarking thing is that the relative density gradually decreased as \times increased.

3.2. Compression test of 4D metamaterials structures

3.2.1. Engineering strain vs Engineering stress

All of the structures were compressed to about 30 % of the original height. Exemplified by structures S-I-1–0.5, S-I-1.5–0.5, and S-I-2–0.5, the typical crushing process was shown in Fig. 6. For a unit cell that made up the structure, the load applied to it was equal when the structure underwent the compressive load, and the collapse usually began with the local buckling of the supporting beam in a single unit-cell layer. During the loading process, the specimens were placed in the center of the testing machine, avoiding odd loads. Accompanied by the buckling vibration, it can be seen that the structure collapsed layer by layer, and the experiments continued until the structure was densified.

For structures S-I-1–0.5, S-II-1–0.5 and S-III-1–0.5, the corresponding relationship between the monotone increasing engineering

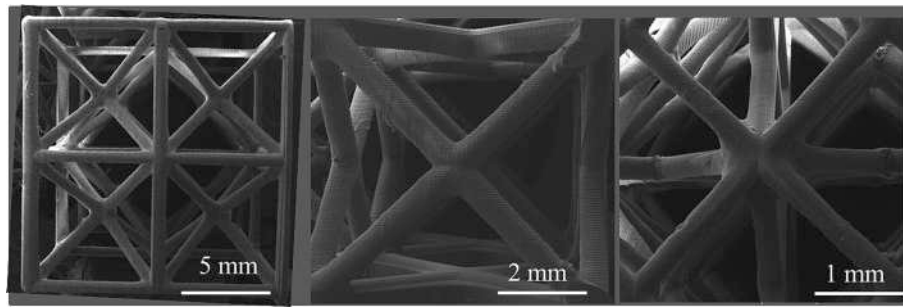


Fig. 5. SEM observations of the fabricated structure.

Table 1
Related physical parameters for *meta*-materials structures.

Specimen	$\bar{\rho}(\%)$	V_m	Mass (g)	Specimen	$\bar{\rho}(\%)$	V_m	Mass (g)
S-I-1-0.5	5.28	8321	9.15	S-I-1-0.75	11.31	17,814	19.59
S-I-1-1	19.09	30,056	33.06	S-I-1.5-0.5	4.25	6692	7.36
S-I-2-0.5	3.78	6608	6.60	S-II-1-0.5	7.93	12,482	13.73
S-II-1-0.75	18.10	15,987	17.58	S-II-1-1	27.74	43,682	48.05
S-II-1.5-0.5	16.40	10,084	11.09	S-II-2-0.5	5.71	9989	10.98
S-III-1-0.5	14.72	7436	8.18	S-III-1-0.75	10.15	28,489	31.33
S-III-1-1	17.21	27,099	29.80	S-III-1.5-0.5	3.82	6008	6.61
S-III-2-0.5	3.39	5931	6.52	S-I-1r	10.70	17,000	18.70
S-II-1r	17.27	27,200	30.00	S-III-1r	10.47	16,500	18.10
S-I-1,1.5,2	4.23	10,000	11.00	S-II-1,1.5,2	7.62	18,000	12.80
S-III-1,1.5,2	4.91	11,600	19.80	S-I, II, III	6.54	10,300	11.30

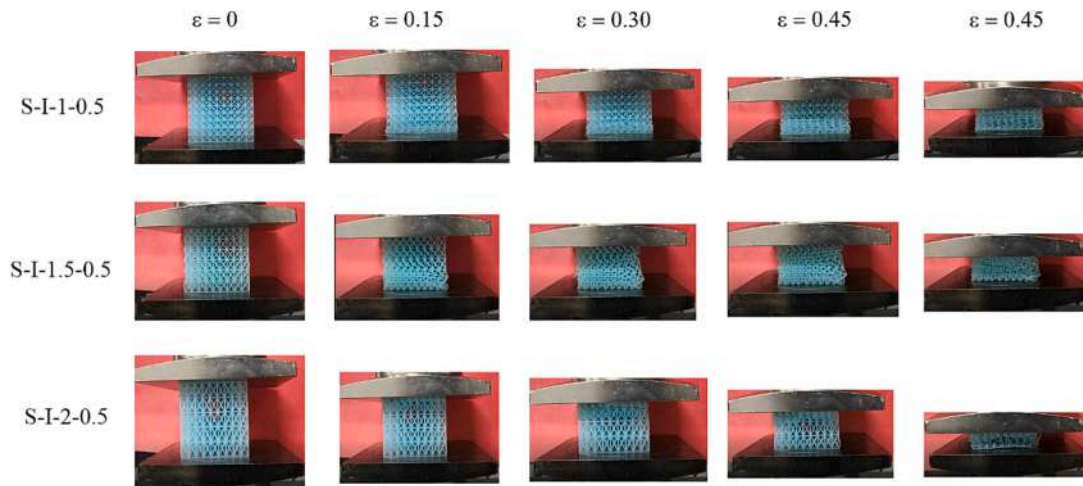


Fig. 6. The typical crushing process for the metamaterials structures.

compression deformation and the peak value of the real-time curve during compression are shown in Fig. 7 (a)-(c). After the initial linear stage, the engineering stress-engineering strain curves presented a weak increasing trend, entering the elastoplastic stage. The peaks in the curves represented the complete collapse of a unit cell at one layer and the beginning of the buckling of the unit cell in the next layer. During the compressive process, the trusses of the unit-cell were mainly subjected to the bending effect, and the first peak stress of each structure was 0.21 MPa, 0.31 MPa, and 0.16 MPa, respectively.

The engineering stress-strain curves for structures with $r = 0.5$ mm in the compression process were shown in Fig. 8. During the elastic loading stage, all specimens rose rapidly to the first initial buckling stress and quickly dropped to about half the original stress. Subsequently, the stress reciprocated within a certain range. The first and the progressive crushing stress limit value of structures S-I, S-II, and S-III increased significantly upon increasing the diameters of the truss. The

increase of the diameter increased the flexural delayed plastic deformation, and this enhancement also provided a noticeable growth in the compressive strength. For the structures with the same type, the order of maximum load from high to low was $X = 1 > X = 1.5 > X = 2$. The larger the ratio of length to height \times was, the more stable the evolution trend of engineering stress with engineering strain was. Additionally, the strength of S-II series was higher than that of S-I and S-III series structures, and the strength of S-III series structures was the lowest.

The engineering stress-engineering strain curves for the structures with a diameter of $r = 0.75$ and $r = 1$ were shown in Fig. 9. The first initial buckling stresses were 1.41 MPa, 1.63 MPa and 1.87 MPa for structures with $r = 0.75$ mm, respectively, which were significantly higher than the structures with a diameter of 0.5 mm. S-II series structures exhibited excellent energy absorption performance, and the stress evolution was relatively stable after reaching the first stress extreme value. For structures with $r = 1$ mm, the first initial buckling stresses

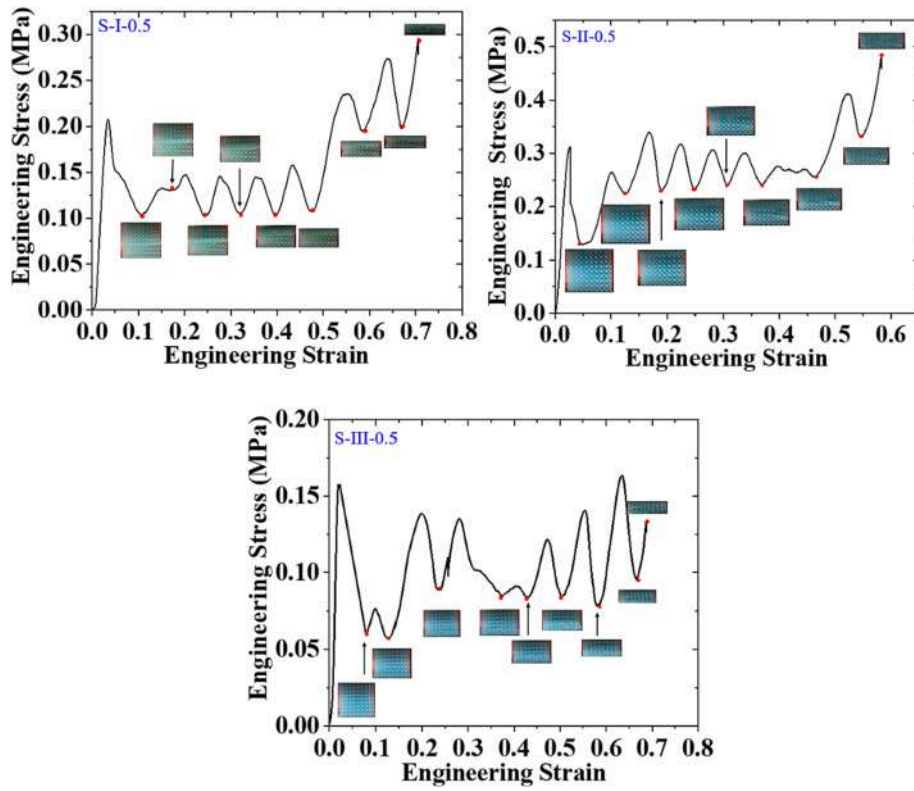


Fig. 7. The engineering stress- engineering strain response of S-I-1-0.5, S-II-1-0.5, and S-III-1-0.5 with weakly damped oscillations.

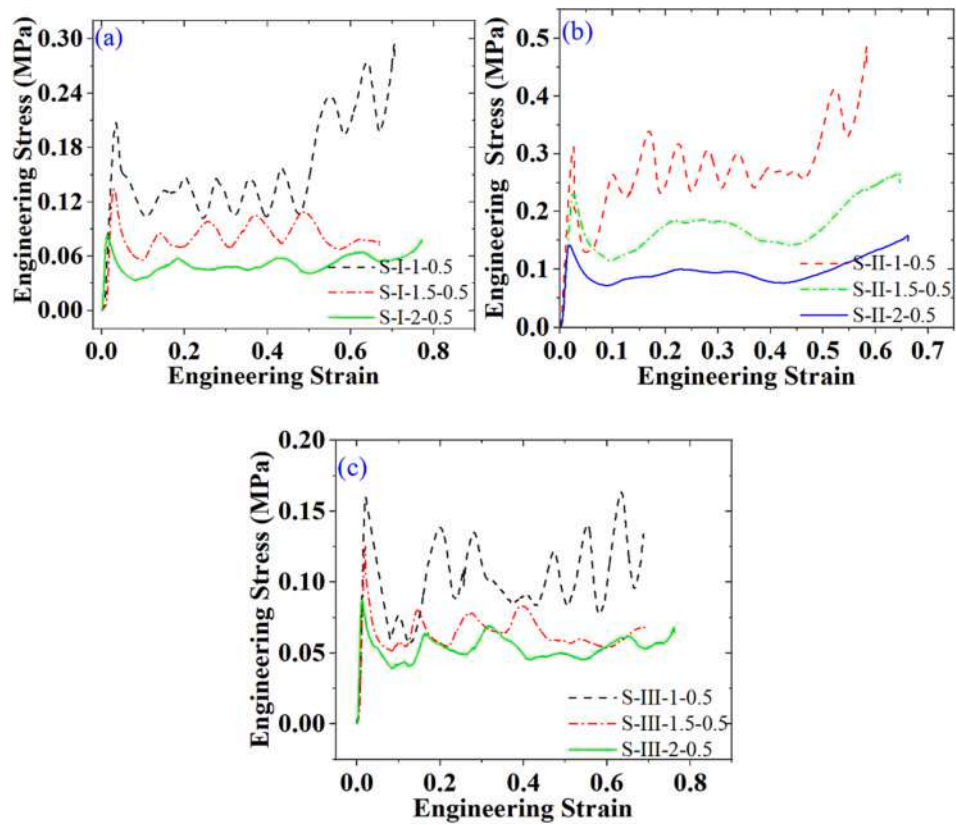


Fig. 8. Engineering strain vs engineering stress of the lattice structures with different length to height ratio (a) S-I (b) S-II (c) S-III.

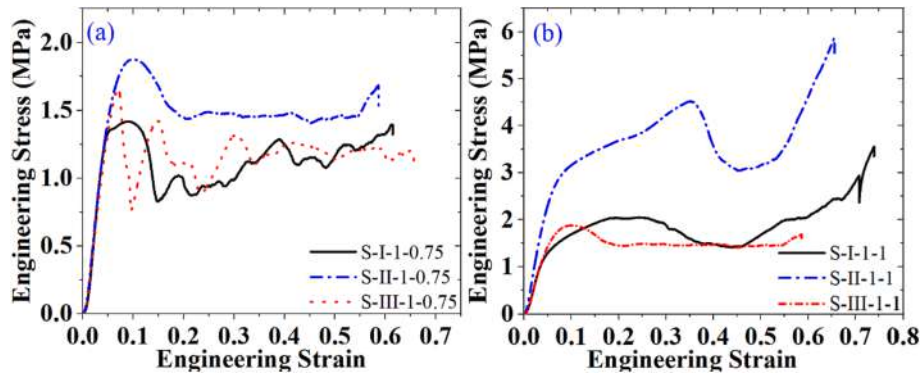


Fig. 9. Engineering strain vs engineering stress of the lattice structures with a diameter of (a) 0.75 mm and (b) 1 mm.

were 3.13 MPa, 2.03 MPa, and 1.87 MPa, respectively. After the load reaching to the first initial buckling stresses, the stress oscillated within a range as the deformation increases. The stress evolution of S-I and S-III series structures was relatively stable, while the stress of the S-II series structure showed a trend of rising-falling- rising with the deformation of 35 % as the boundary. The increase in truss diameter increased the bending resistance of the structure and greatly improved the overall strength of the structure. Among the three configurations, structure S-II exhibited a stronger compressive resistance, which can be attributed to that structure S-II has more triangular elements along the direction of loading. This fully proves that the dissipative capacity of the structure can be further improved by reasonable structural design as mentioned above.

The engineering stress-engineering strain responses of the gradient structures were shown in Fig. 10. The stress evolution trend of S-I, S-II and S-III series structures exhibited an obvious step change when the diameter of the truss was a gradient, corresponding to $r = 0.5$ mm, $r = 0.75$ mm and $r = 1$ mm, respectively, as shown in Fig. 10(a). However,

there was no significant step change for engineering stress-engineering strain responses of structures with the gradient change in the ratio of length and height as illustrated in Fig. 10(b). The mechanical performances of the structure comprised of unit-cell S-I, S-II, and S-III were shown in Fig. 10(c). The mechanical response exhibited step change with the increase of deformation, corresponding to S-III-1-0.5, S-I-1-0.5 and S-II-1-0.5.

3.2.2. Crushing parameters of the meta-materials

Fig. 11 illustrated the relevant parameters of the compression performance, in which EA and SEA increased upon increasing the truss's diameter. With the beam's diameter increasing from 0.5 mm to 1 mm, SEA increased more than 10 times. It can be observed that the mechanical strength and stiffness of S-II series structures were the best while there was little difference in the mechanical properties between S-I and S-III. The SEA of S-II was the highest, while the SEA of S-I and S-III were comparable. In particular, when the structure had almost the same quality, the SEA of structure S-II was 32.6 % and 26.9 % higher than S-I

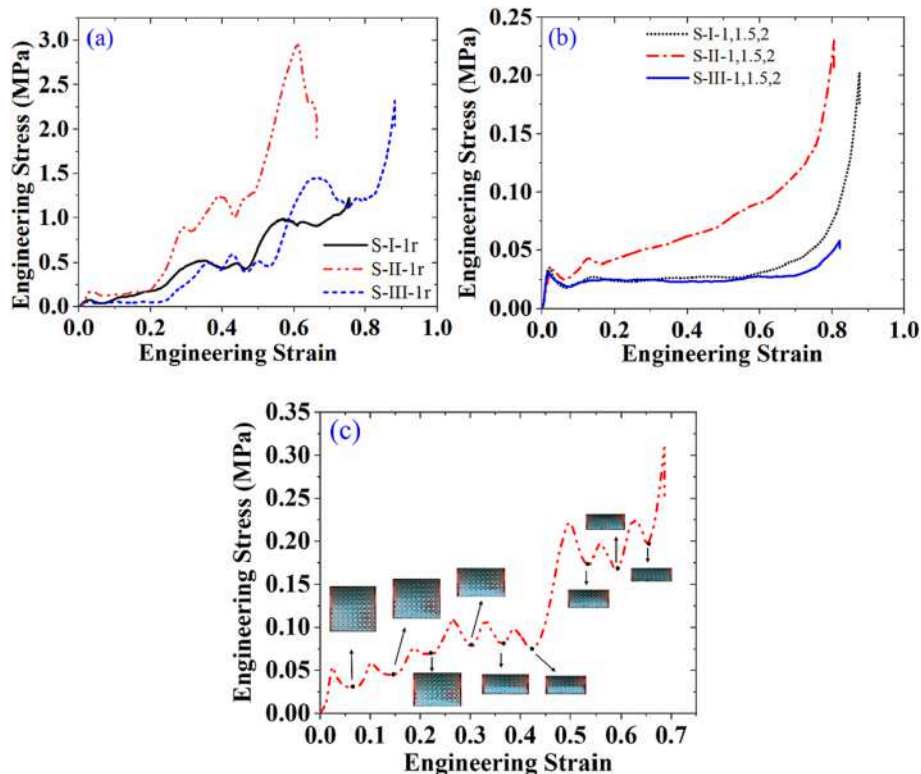


Fig. 10. Engineering strain vs engineering stress of the gradient structures (a) Gradient change in diameter (b) Gradient change in the ratio of length and height (c) Gradient variation of the unit-cell type.

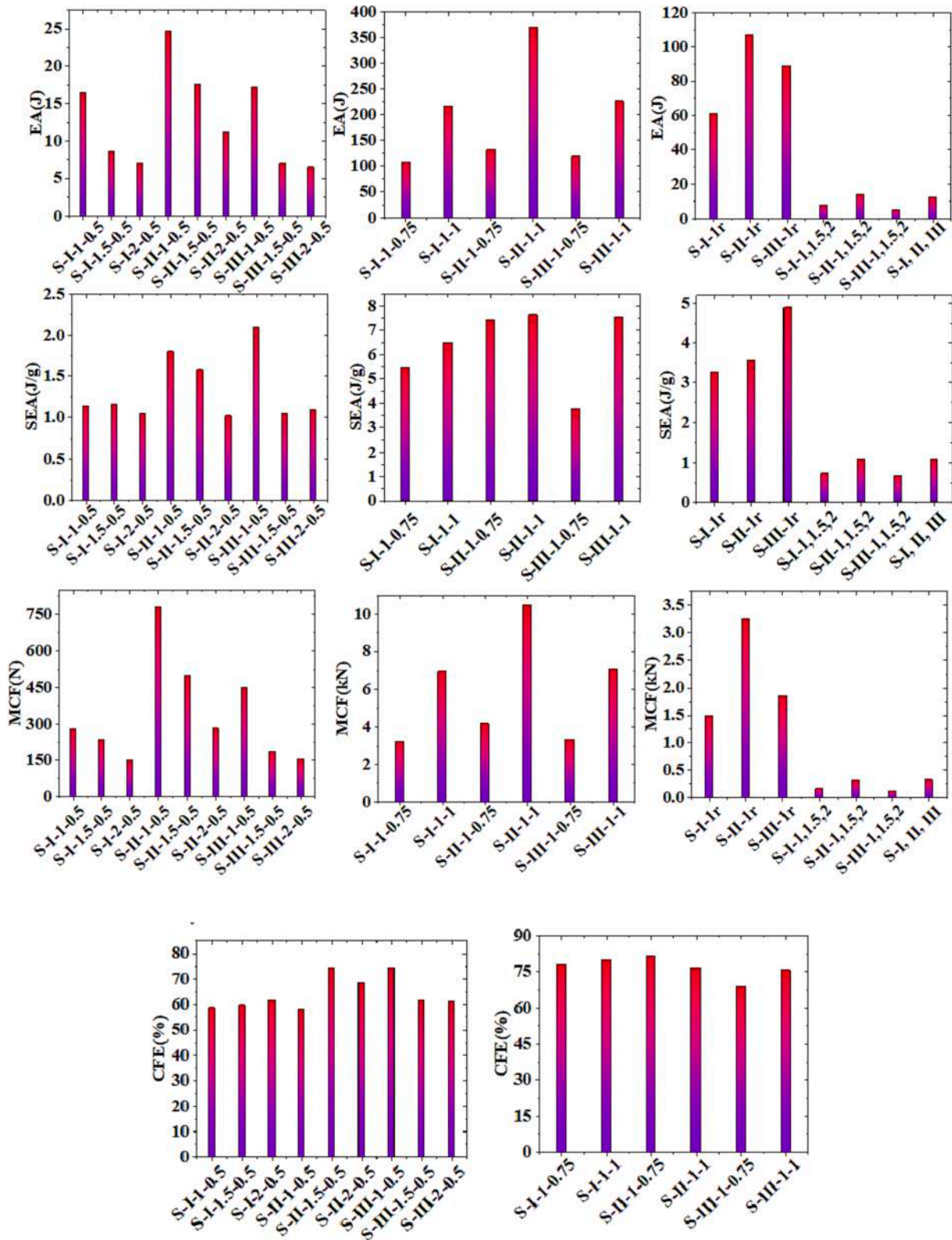


Fig. 11. Crashing performance parameters for *meta*-materials structures.

and S-II, respectively. We can find that the diameter of the truss was an effective parameter to increase the SEA of the structures. Furthermore, the increase in the ratio of length to the unit cell's height increased the structure's porosity, but the SEA was weakened.

MCF was directly dependent on total energy absorption. Consequently, the effect of unit-cell geometry, the truss diameter, and the rate

of length and height on MCF were the same as those of EA and SEA. CFE was an essential parameter to evaluate the crushing properties of *meta*-materials, which indicated the uniformity of the stress-strain curve. A larger CFE means the energy can be dissipated more efficiently. CFE gradually increased with the increase of the truss's diameter. However, the higher ratio between the length to height, the smaller of CFE.

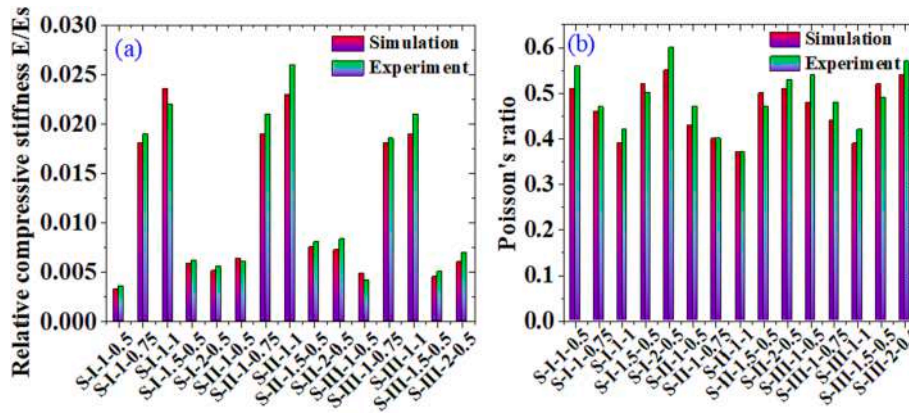


Fig. 12. Comparisons of simulation and experiments of (a) Relative compressive stiffness and (b) Poisson's ratio.

3.2.3. Mechanical properties of the meta-materials

The comparisons between the simulation and experiments of the mechanical properties were demonstrated in Fig. 12. The simulated results agreed well with the experimental ones. From Fig. 12(a), it can be obtained that the relative compressive stiffness increase with the increase of the truss's diameter. Besides, the ratio between the height and the length of the unit cell can effectively affect the value of the relative stiffness. The higher the ratio, the greater the relative stiffness. It was worth noting that S-II had the largest relative stiffness compared with the other two structures. The Poisson's ratio was sensitive to the change of the parameters including the diameters of the truss and different ratios of length and height. As shown in Fig. 12(b), the Poisson's ratio decreases gradually upon increasing the truss's diameters. Additionally, Poisson's ratio increased gradually upon increasing the ratio between length and height. However, the value of Poisson's ratio did not differ much among the three structures with different types of unit-cell.

3.2.4. Shape memory behavior

The shape memory cycle test was shown in Fig. 13, and its four stages are as follows. The temperature was first heated to 90 °C and maintained for 5 min to reach thermal equilibrium. Subsequently, 50 % deformation was applied to the metamaterials. The third stage was to cool the temperature from 90 °C to 20 °C with a rate of 2.5 °C/min. After that, the external force was unloaded while retaining the deformation. The last stage was reheating the temperature from 20 °C to 90 °C with a rate of 2.5 °C/min. The metamaterial recovered to its initial configuration gradually upon increasing the temperature. The comparisons between simulation and experiment in the shape recovery process were shown in

Fig. 13(a). The deformation-load response changing with the temperature is shown in Fig. 13(b). After a thermal-mechanical cycle, the metamaterial recovered to its initial shape. Furthermore, utilizing fused deposition modeling and shape memory PLA/Fe₃O₄, we fabricate a series of mechanical metamaterials, and the shape memory behavior was verified actuated by a magnetic field (Supporting Information).

4. Conclusions

In summary, combined with the bionic design, we designed a stretching-dominated metamaterial, which was ultralight, had high strength, and had high specific energy absorption efficiency with low relative density. By controlling the topological parameters, the mechanical performance of the lattice metamaterials can be adjusted accordingly. The experimental results indicated that the lattice metamaterials had high specific strength. The design of the functionally graded structures with gradient mechanical properties highlighted their potential applications in tissue engineering and the shock absorption field. In addition, the introduction of the shape memory function enables the structure to have the function of shape transition, which provides the possibility of application in the field of tissue stents and is immensely convenient for the operation of minimally invasive surgery.

Author statement.

Prof. Jinsong Leng and Yanju Liu directed the research. Wei Zhao conceived and designed the structures, performed all the characterization and wrote the manuscript. Prof. Liwu Liu directed the analyses of the stent properties. Cheng Binyue Finished the experiments of the structures. All authors have given approval to the final version of the

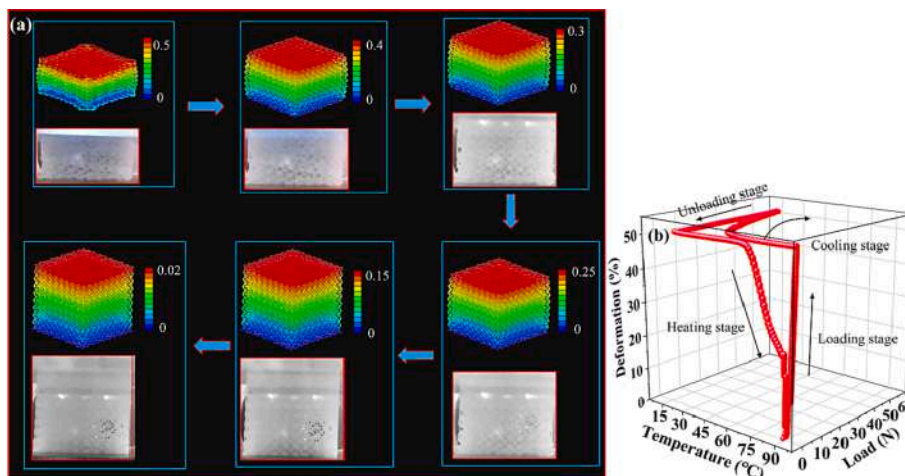


Fig. 13. Shape-transformation of lattice metamaterials (a) Comparisons between simulation and experiment (b) Deformation-load-temperature curve.

manuscript.

Declaration of Competing Interest

The authors declare that they have no known competing financial interests or personal relationships that could have appeared to influence the work reported in this paper.

Data availability

Data will be made available on request.

Acknowledgements

This work was supported by the National Natural Science Foundation of China (Grant No. 12072094 and 12172106), Heilongjiang Touyan Innovation Team Program, the Fundamental Research Funds for the Central Universities (No. IR2021106 and IR2021232).

Appendix A. Supplementary material

Supplementary data to this article can be found online at <https://doi.org/10.1016/j.compstruct.2022.116360>.

References

- Nicolaou ZG, Motter AE. Mechanical metamaterials with negative compressibility transitions. *Nat Mater* 2012;11(7):608–13.
- Klatt T, Haberman MR. A nonlinear negative stiffness metamaterial unit cell and small-on-large multiscale material model. *J Appl Phys* 2013;114(3):167–207.
- Xu Y, Schlangen E, Luković M, Šavija B. Tunable mechanical behavior of auxetic cementitious cellular composites (CCCs): Experiments and simulations. *Constr Build Mater* 2021;266:121388.
- Yasuda H, Yang J. Reentrant Origami-Based Metamaterials with Negative Poisson's Ratio and Bistability. *Phys Rev Lett* 2015;114(18):185502.
- Mirzaali MJ, Janbaz S, Strano M, Vergani L, Zadpoor AA. Shape-matching soft mechanical metamaterials. *Sci Rep* 2018;8(1):1–7.
- Dudek KK, Gatt R, Dudek MR, Grima JN. Negative and positive stiffness in auxetic magneto-mechanical metamaterials. *P Roy Soc A-Math Phys* 2018;474(2215): 20180003.
- Mirzaali MJ, Habibi M, Janbaz S, Vergani L, Zadpoor AA. Crumpling-based soft metamaterials: the effects of sheet pore size and porosity. *Sci Rep* 2017;7(1):1–7.
- Fan H, Hartshorn C, Buchheit T, Tallant D, Assink R, Simpson R, et al. Modulus–density scaling behaviour and framework architecture of nanoporous self-assembled silicas. *Nat Mater* 2007;6(6):418–23.
- Palucka T. Mechanical metamaterials produce ultralight, ultra stiff lattices. *MRS Bull* 2014;39(9):759–60.
- Jang W-Y, Kyriakides S, Kraynik AM. On the compressive strength of open-cell metal foams with Kelvin and random cell structures. *Int J Solids Struct* 2010;47(21):2872–83.
- Wei ZY, Guo ZV, Dudte L, Liang HY, Mahadevan L. Geometric mechanics of periodic pleated origami. *Phys Rev Lett* 2013;110(21):325–9.
- Traugutt NA, Mistry D, Luo CQ, Yu K, Ge Q, Yakacki CM. Liquid-crystal-elastomer-based dissipative structures by digital light processing 3D printing. *Adv Mater* 2020;32(28):2000797.
- Luo CQ, Chung C, Traugutt NA, Yakacki CM, Long KN, Yu K. 3D printing of liquid crystal elastomer foams for enhanced energy dissipation under mechanical insult. *ACS Appl Mater Inter* 2021;13(11):12698–708.
- Mistry D, Traugutt NA, Sanborn B, Volpe RH, Chatham LS, Zhou R, et al. Soft-elasticity optimises dissipation in 3D-printed liquid crystal elastomers. *Nat Commun* 2021;12(1):6677.
- Mines RAW, Tsoupanos S, Shen Y, Hasan R, McKown ST. Drop weight impact behaviour of sandwich panels with metallic micro lattice cores. *Drop weight impact behaviour of sandwich panels with metallic micro lattice cores* 2013;60: 120–32.
- Tancogne-Dejean T, Spierings AB, Mohr D. Additively-manufactured metallic micro-lattice materials for high specific energy absorption under static and dynamic loading. *Acta Mater* 2016;116:14–28.
- Deshpande VS, Ashby MF, Fleck NA. Foam topology bending versus stretching dominated architectures. *Acta Mater* 2001;49(6):1035–40.
- Schaedler TA, Jacobsen AJ, Torrents A, Sorensen AE, Lian J, Greer JR, et al. Ultralight metallic microlattices. *Science* 2011;334(6058):962–5.
- Yuan S, Chua CK, Zhou K. 3D-Printed Mechanical Metamaterials with High Energy Absorption. *3D-printed mechanical metamaterials with high energy absorption* 2019;4(3):1800419.
- Kephardt JO. Learning from nature. *Science* 2011;331(6018):682–3.
- Zhao W, Liu L, Leng J, Liu Y. Thermo-mechanical behavior prediction of shape memory polymer based on the multiplicative decomposition of the deformation gradient. *Mech Mater* 2020;143:103263.
- Hanson DW, Lu H, Yakacki CM, Yu K. Influence of mechanically-induced dilatation on the shape memory behavior of amorphous polymers at large deformation. *Mech Time-Dependent Mater* 2019;23(1):1–21.
- Wang XD, Lu HB, Shi XJ, Yu K, Fu YQ. A thermomechanical model of multi-shape memory effect for amorphous polymer with tunable segment compositions. *Compos Part B-Eng* 2019;160:298–305.
- Zhao W, Liu LW, Zhang FH, Leng JS, Liu YJ. Shape memory polymers and their composites in biomedical applications. *Mater Sci Eng C-Mater Biol Appl* 2019;97: 864–83.
- Mao YQ, Chen F, Hou SJ, Qi HJ, Yu K. A viscoelastic model for hydrothermally activated malleable covalent network polymer and its application in shape memory analysis. *J Mech Phys Solids* 2019;127:239–65.
- Zhao W, Huang ZP, Liu LW, Wang WB, Leng JS, Liu YJ. Bionic design and performance research of tracheal stent based on shape memory polycaprolactone. *Compos Sci Technol* 2022;229(20):109671.
- Zhao W, Liu L, Leng J, Liu Y. Thermo-mechanical behavior prediction of particulate reinforced shape memory polymer composite. *Compos Part B Eng* 2019; 179:107455.
- Murcia Morales M, Gómez Ramos MJ, Parrilla Vázquez P, Díaz Galiano FJ, García Valverde M, Gámiz López V, et al. Distribution of chemical residues in the beehive compartments and their transfer to the honeybee brood. *Sci Total Environ* 2020; 710:136288.
- Bertoldi K, Boyce MC, Deschanel S, Prange SM, Mullin T. Mechanics of deformation-triggered pattern transformations and superelastic behavior in periodic elastomeric structures. *J Mech Phys Solids* 2008;56(8):2642–68.
- Wu GX, Xia Y, Yang S. Buckling, symmetry breaking, and cavitation in periodically micro-structured hydrogel membranes. *Soft Matter* 2014;10(9):1392–9.
- Zhang Y, Matsumoto EA, Peter A, Lin PC, Kamien RD, Yang S. One-step nanoscale assembly of complex structures via harnessing of elastic instability. *Nano Lett* 2008;8:1192–6.
- Yuan C, Mu XM, Dunn CK, Haidar J, Wang TJ, Qi HJ. Thermomechanically triggered two-stage pattern switching of 2D lattices for adaptive structures. *Adv Funct Mater* 2018;28(18):1705727.
- Zhang Q, Yan D, Zhang K, Hu GK. Pattern transformation of heat-shrinkable polymer by three-dimensional (3D) printing technique. *Sci Rep* 2015;5(1):1–6.
- Zhao W, Zhu J, Liu L, Leng J, Liu Y. Analysis of small-scale topology and macroscale mechanical properties of shape memory chiral-lattice metamaterials. *Compos Struct* 2021;262:113569.
- Zhao W, Li N, Liu L, Leng J, Liu Y. Origami derived self-assembly stents fabricated via 4D printing. *Compos Struct* 2022;293:115669.
- Zhao W, Zhang F, Leng J, Liu Y. Personalized 4D printing of bioinspired tracheal scaffold concept based on magnetic stimulated shape memory composites. *Compos Sci Technol* 2019;184:107866.
- Zhao W, Huang Z, Liu L, Wang W, Leng J, Liu Y. Porous bone tissue scaffold concept based on shape memory PLA/Fe₃O₄. *Compos Sci Technol* 2021;203: 108563.
- Ansari S, Khorshidi S, Karkhaneh A. Engineering of gradient osteochondral tissue: From nature to lab. *Acta Biomater* 2019;87:41–54.
- Wang ZG, Liu JF. Mechanical performance of honeycomb filled with circular CFRP tubes. *Compos Part B-Eng* 2018;135:232–41.
- Paz J, Diaz J, Romera L, Costas M. Crushing analysis and multi-objective crashworthiness optimization of GFRP honeycomb-filled energy absorption devices. *Finite Elem Anal Des* 2014;91:30–9.
- Zuhri MYM, Guan ZW, Cantwell WJ. The mechanical properties of natural fibre based honeycomb core materials. *Compos Part B-Eng* 2014;58:1–9.